ADVANCED PHYSICS RESEARCH Open Access
www.advphysicsres.com

Magnetic-Field Induced Charge Accumulation in Scalable Magnetoelectric PVDF-TrFE/Ni Composite Devices

*Federica Luciano, Erika Giorgione, Emma Van Meirvenne, Andrei Galan, Ilaria Marzorati, Arne De Coster, Dominika Wysocka, Bart Sorée, Stefan De Gendt, Florin Ciubotaru, and Christoph Adelmann**

This study investigates the direct magnetoelectric effect in thin film composites comprising a 550 nm thick poly(vinylidene fluoride-trifluoroethylene) (PVDF-TrFE) layer spin-coated onto a 500 µm thick Ni foil substrate. Direct measurements of charge accumulation on dot capacitors with Au top electrodes, induced by the rotation of Ni magnetization from in-plane to out-of-plane orientation by an applied magnetic field, reveal pronounced magnetoelectric coupling. Polarization differences between in-plane and out-of-plane magnetization states of up to $(13.8 \pm 0.8) \times 10^{-4}$ µC cm^{-2} are derived from charge measurements. This corresponds to a maximum open circuit voltage difference of up to 75 ± 6 mV and a magnetoelectric coupling coefficient with respect to magnetization changes of 310 ± 27 mVA^{-1}. Finite element simulations using COMSOL Multiphysics corroborate experimental findings, indicating near-independence of generated polarizations and open circuit voltages when lateral capacitor dimensions are reduced into the nanometer range. Simulations of nanoscale pillar devices on rigid substrates, employing materials with optimized piezoelectric and magnetostrictive parameters, predict the potential for generating large open circuit voltage differences exceeding 2 V, highlighting the prospects of such devices for spintronic applications.

1. Introduction

Magnetoelectrics are materials that exhibit an intrinsic coupling between electric polarization and (ferromagnetic) magnetization.[1–7] This coupling enables the manipulation of the material's magnetic properties using an external voltage, or conversely, the control of polarization via an external magnetic field. This dual functionality has garnered considerable attention from both fundamental and applied research perspectives.[6,8–11] Recent efforts have increasingly focused on leveraging magnetoelectric phenomena for microelectronic device applications, including logic gates, memory cells, or magnetic sensors.[6,9–11] The converse magnetoelectric effect, in particular, promises to enable low-voltage magnetization manipulation of nanomagnets at much lower power than methods using, e.g., spin-transfer or spin-orbit torques.[9–14] Alternatively, the direct magnetoelectric effect may be used to read the magnetization state of a nanomagnet, potentially generating large polarizations equivalent to voltages that significantly exceed those achievable, e.g., through inverse spin-Hall effect-based detection schemes.

Magnetoelectric materials encompass single-phase multiferroics, which simultaneously exhibit ferroelectric and (anti-)ferromagnetic ordering.[5,15–18] However, the scarcity of room-temperature multiferroics,[19] primarily limited to $BiFeO_3$ with its relatively weak intrinsic coupling,[20] has spurred interest in composite systems.[1,4,6,21–24] Such magnetoelectric composites, composed of piezoelectric and ferromagnetic magnetostrictive phases,

F. Luciano, E. Giorgione, E. Van Meirvenne, A. Galan, I. Marzorati, A. De Coster, D. Wysocka, B. Sorée, S. De Gendt, F. Ciubotaru, C. Adelmann
imec
Leuven 3001, Belgium
E-mail: christoph.adelmann@imec.be
F. Luciano, S. De Gendt
Department of Chemistry
KU Leuven
Leuven 3001, Belgium

The ORCID identification number(s) for the author(s) of this article can be found under https://doi.org/10.1002/apxr.202400158

DOI: 10.1002/apxr.202400158

E. Giorgione
Department of Electronics and Telecommunications (DET)
Politecnico di Torino
Turin 10129, Italy
E. Van Meirvenne, A. De Coster, B. Sorée
Department of Electrical Engineering (ESAT)
KU Leuven
Leuven 3001, Belgium
A. Galan
Department of Electrical Engineering
Université de Liège
Liège 4000, Belgium
I. Marzorati
Department of Chemistry
Materials and Chemical Engineering
Politecnico di Milano
Milan 20133, Italy

often demonstrate substantially larger coupling strengths. In these systems, the magnetoelectric coupling is mediated by strain, induced either through piezoelectric actuation by applied electric fields (converse magnetoelectric effect) or magnetostrictive response by applied magnetic fields (direct magnetoelectric effect). Among these composites, piezoelectric/magnetostrictive bilayers represent the simplest and most studied systems.

Much progress has been achieved in recent years concerning the efficient electrical manipulation of ferromagnets via the converse magnetoelectric effect.[10,14,25] Magnetoelectric composites with large coupling coefficients have been reported, which enables the manipulation of their magnetization under the application of low electric fields.[25–29] Additionally, exchange-coupled bilayers comprising multiferroic $BiFeO_3$ and ferromagnetic thin films (e.g., CoFe) have demonstrated low switching voltages down to 150 mV due to the utilization of ultrathin multiferroic films.[10,14,30,31] Nonetheless, a key remaining issue consists of downscaling these devices to dimensions compatible with microelectronic applications.

In contrast, the generation of charge or polarization (voltage) in thin film devices from external magnetic fields via the direct magnetoelectric effect remains a formidable challenge. To date, experimental demonstrations utilizing thin films of single-phase multiferroics like $BiFeO_3$ have been elusive. While the direct magnetoelectric effect in magnetoelectric composites has been extensively studied,[4,32,33] device miniaturization represents a significant challenge, hindered by measurement sensitivity limitations at small scales. Advancements in this area could become particularly enabling for low-power spintronic applications,[34,35] where conventional readout methods, such as tunnel magnetoresistance or inverse spin-Hall effect, suffer from high power consumption[36] or low generated voltages,[9,37–41] respectively.

In this work, we present an investigation of the magnetoelectric coupling in poly(vinylidene fluoride-trifluoroethylene) (PVDF-TrFE)/Ni bilayer composites through direct measurement of charge accumulation induced by magnetization rotation from in-plane to out-of-plane orientation. This configuration mitigates the influence of domain formation in larger in-plane magnetized devices and superparamagnetism in smaller structures, hence improving scalability. Experimental results demonstrate polarization differences of up to 13.8×10^{-4} μCcm^{-2} between in-plane and out-of-plane magnetization states, corresponding to an open circuit voltage difference of 75 mV. Finite element simulations corroborate the experimentally determined charge and polarization values and predict the scalability of the device to the nanometer regime without significant performance degradation. Furthermore, simulations indicate that optimized material selection and device geometry can yield nanoscale magnetoelectric composite devices on Si substrates polarizations equivalent to open circuit voltage differences of more than 2 V.

2. Experimental Investigation of Magnetoelectric Coupling in PVDF-TrFE/Ni Bilayer Composites

2.1. Sample Preparation and Magnetoelectric Composite Characteristics

This study investigates the direct magnetoelectric effect in composite structures comprising magnetostrictive nickel (Ni) foils and piezoelectric PVDF-TrFE thin films. Amongst the copolymers of poly(vinylidenefluoride) (PVDF), PVDF-TrFE stands out due to its strongly enhanced piezoelectric response.[42] **Figure 1**a illustrates the fabrication process for the investigated devices. A 550 nm thick PVDF-TrFE layer was spin-coated onto a 500 μm thick self-supporting Ni foil substrate, followed by thermal evaporation of a 200 nm Au film through a shadow mask to define Au dot electrodes with diameters ranging from 200 to 750 μm. Figure 1b presents a micrograph of multiple dot capacitor devices of varying diameters. Atomic force microscopy (AFM) analysis of the PVDF-TrFE surface morphology, as depicted in Figure 1c, revealed a uniform and pinhole free layer with a relatively low root mean square (RMS) roughness of 3.5 nm.

Ferromagnetic properties of the Ni foils were characterized using vibrating sample magnetometry (VSM). **Figure 2**a,b show magnetization versus applied magnetic field curves for in-plane and out-of-plane configurations, respectively. The in-plane hysteresis loop exhibited minimal coercivity (≈1.5 mT) and negligible remanence, indicative of magnetic domain formation at low field strengths. Above ≈50 mT, the magnetization saturated at M_s = 440 kA/m, consistent with bulk Ni.[43] By contrast, significantly higher out-of-plane magnetic fields of 0.6 T were necessary to reach saturation due to substantial demagnetizing field effects, i.e., due to shape anisotropy, in this configuration.

As-deposited PVDF-TrFE films crystallize in the nonferroelectric α-phase. Therefore, the films must be transformed into the ferroelectric β-phase, which generates spontaneous polarization by forming electric dipoles perpendicular to the chain direction.[42,44] Figure 2c schematically illustrates the polymer chain conformations of the α- and β-phases for PVDF. The α-phase exhibits a TGTG (trans-gauche-trans-gauche) conformation, while the ferroelectric β-phase adopts a TTTT (trans-trans-trans-trans) configuration, which leads to electric dipole formation. The transformation into the β-phase was achieved through AC poling using 200 triangular pulses (80 V peak-to-peak) at 50 Hz.[45]

The ferroelectric properties of the PVDF-TrFE films were characterized through polarization versus applied electric field (P–E) hysteresis loop measurements. The measurements were carried out for each dot diameter and are reported in Figure 2d, showing clear ferroelectric hysteresis. The observed coercive field (E_c) was ≈450 kVcm^{-1}, with remnant polarization (P_r) and saturation polarization (P_s) values of 6.0 ± 0.5 μCcm^{-2} and 7.2 ± 0.5 μCcm^{-2}, respectively. These ferroelectric parameters showed only a weak dependence on the dot diameter and were consistent with previously reported values for PVDF-TrFE films.[46,47] This suggests a high β-phase content within the PVDF-TrFE films on Ni foils after poling.[48]

In addition, capacitance–voltage (C–V) hysteresis loops were measured for devices of various dot dimensions and are presented in Figure 2e. These measurements were conducted at a frequency of 10 kHz, revealing characteristic butterfly-shaped loops when sweeping the DC bias voltage between −35 and 35 V. The measured capacitance per area exhibited minor variation between different dots. The relative dielectric constant κ of the PVDF-TrFE layer was estimated from the experimentally determined capacitance C. The κ values at zero bias ranged from 10.8 to 11.9, consistent with previously reported values for β-phase PVDF-TrFE.[47,48] Minor variations in κ between different dots

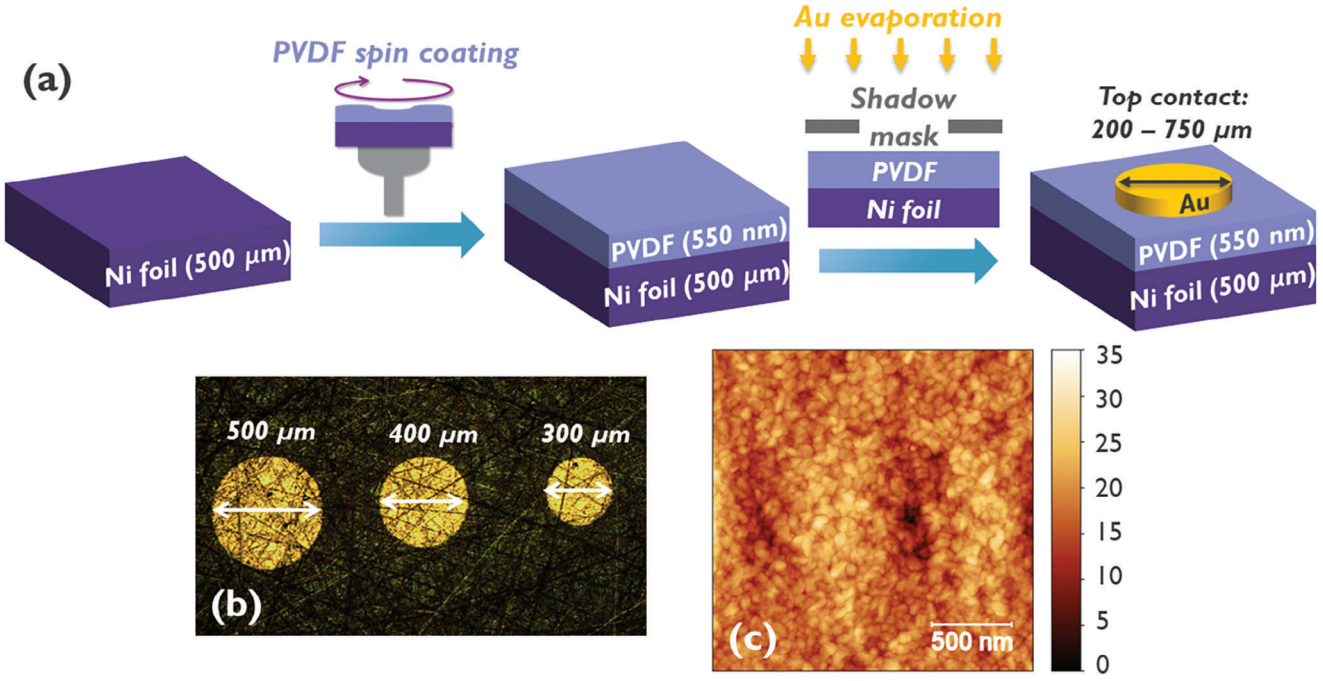

Figure 1. a) Schematic representation of the device fabrication process. The studied magnetoelectric composite devices consist of a Ni foil, a PVDF-TrFE thin film, and a patterned Au top electrode forming an array of dot capacitors. b) Optical micrograph of the fabricated devices with top electrode dots of varying diameters. c) AFM image of the surface morphology of the PVDF-TrFE layer deposited on the Ni foil.

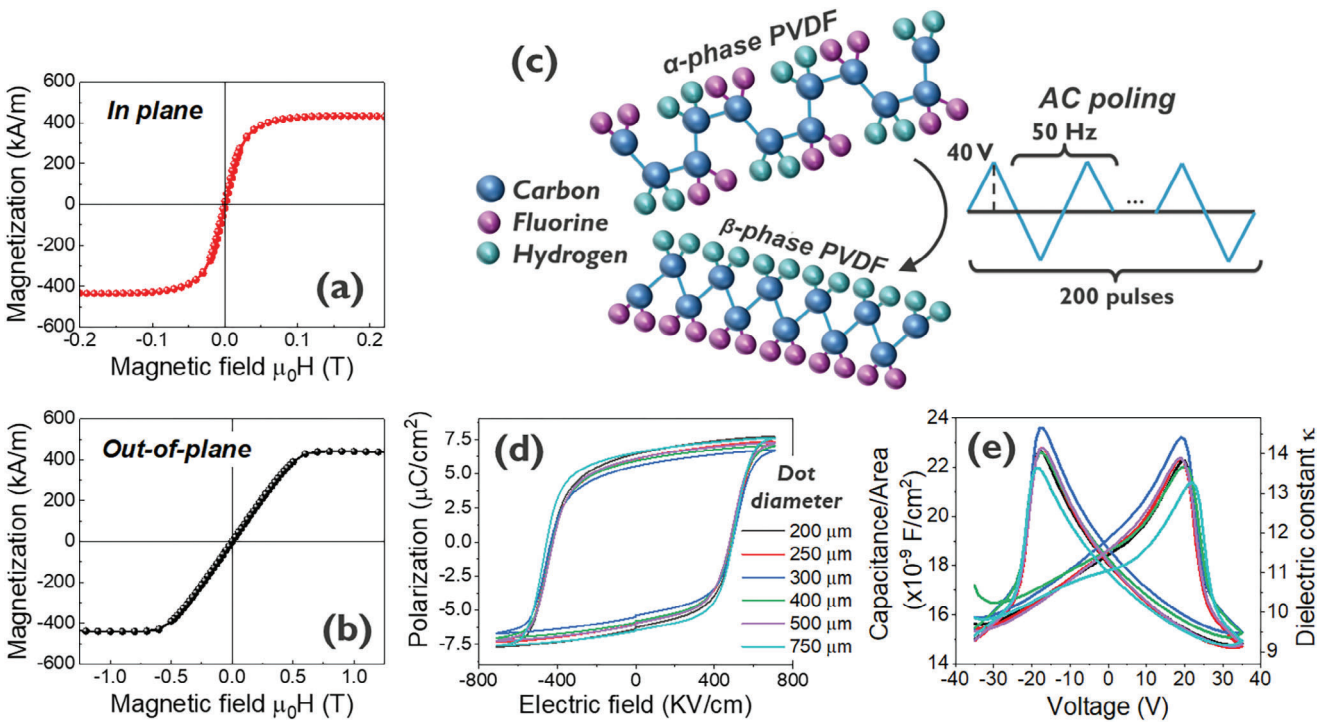

Figure 2. a) In-plane and b) out-of-plane magnetic hysteresis (*M*–*H*) loops of Ni foils measured by VSM. c) Schematic illustration of the AC poling process inducing the phase transition from the non-polar α- to the ferroelectric β-phase of PVDF. d) Polarization versus applied electric field (*P*–*E*) hysteresis loops of 550 nm thick PVDF-TrFE films for varying Au top electrode dot diameters. e) Capacitance versus applied voltage (*C*–*V*) and dielectric constant versus applied voltage (κ–V) hysteresis loops of 550 nm thick PVDF-TrFE films with varying Au top electrode dot diameters. The characteristic butterfly loops and overlapping curves confirm the ferroelectric nature of the material and the consistency across different dot sizes.

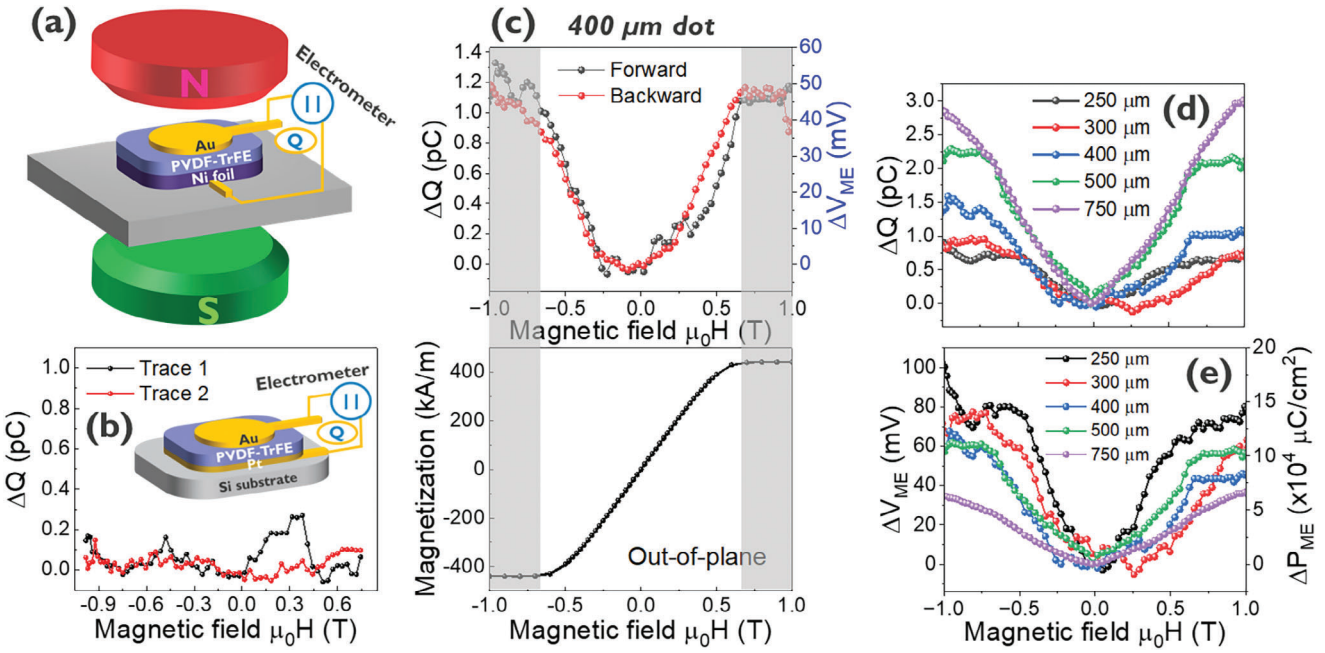

Figure 3. a) Schematic representation of the magnetoelectric measurement setup and magnetic field configuration. b) Charge accumulation (ΔQ) as a function of magnetic field for a PVDF-TrFE/Pt/Si capacitor, demonstrating negligible charge generation in the absence of a magnetostrictive layer. c) ΔQ as a function of magnetic field for a PVDF-TrFE/Ni capacitor, overlaid with the out-of-plane magnetization curve of the Ni foil. The correlation between charge saturation and magnetization saturation can be clearly seen. d) ΔQ as a function of magnetic field for different device dimensions. e) Deduced open circuit voltage and polarization differences as a function of magnetic field for different device dimensions.

can be attributed to thickness fluctuations, dot area measurement errors, and/or β-phase contents.

2.2. Magnetoelectric Effect in PVDF-TrFE/Ni Composites

The magnetoelectric response of the PVDF-TrFE/Ni bilayers was evaluated by quantifying the charge accumulation under applied DC magnetic fields ranging from −1 to 1 T, perpendicular to the sample plane. **Figure 3a** illustrates the experimental configuration. Compared to previously employed AC measurements in the small signal regime,[49–52] DC charge measurements offer enhanced immunity to artifacts, e.g., due to induction,[53] and provide direct access to electrical parameters like generated polarization. As a control experiment, PVDF-TrFE films deposited on a Si (100) substrate with a 100 nm Pt bottom electrode and identical Au top electrodes exhibited negligible charge accumulation above the noise floor (Figure 3b), consistent with the absence of magnetoelectric coupling in this nonmagnetic stack.

In contrast, PVDF-TrFE/Ni samples exhibited clear charge accumulation indicative of a magnetoelectric response. Figure 3c shows representative data for a 400 μm diameter dot. When the applied magnetic field was swept from 0 T to 1 T, the magnetization progressively reoriented out of the plane, saturating at ≈0.6 T. This magnetization rotation induced strain ϵ within the Ni foil via magnetostriction, described by:

$$\epsilon^{m}_{ME} = \frac{3}{2}\begin{pmatrix} \lambda_{100}m_x^2 - \frac{1}{3} & \lambda_{111}m_xm_y & \lambda_{111}m_xm_z \\ \lambda_{111}m_ym_x & \lambda_{100}m_y^2 - \frac{1}{3} & \lambda_{111}m_ym_z \\ \lambda_{111}m_zm_x & \lambda_{111}m_zm_y & \lambda_{100}m_z^2 - \frac{1}{3} \end{pmatrix} \quad (1)$$

where $m = \{m_x, m_y, m_z\}$ is the normalized magnetization direction vector and λ_{100} and λ_{111} denote the saturation magnetostriction coefficients in the respective crystallographic directions for fcc Ni. A detailed discussion of the generated spatial strain distribution using finite element simulations will follow in the next section.

The transferred strain induces a piezoelectric polarization within the PVDF-TrFE film, resulting in the development of an open-circuit voltage. When the capacitor's electrodes are connected, either through the electrometer circuit or intrinsic leakage pathways, the device functions as a transient current source and charge accumulates on the electrodes to compensate for the piezoelectric polarization. By integrating the measured current through the electrometer, the polarization change can be quantified, similar to standard ferroelectric polarization measurements. We note that direct open-circuit voltage measurements in practical piezoelectric sensors are hindered by inevitable leakage currents, leading to transient voltage buildup. Consequently, charge measurements are generally favored over direct voltage measurements for (quasi-)static excitations.[54]

Measurements performed for both positive and negative magnetic fields, as well as with increasing and decreasing magnetic field sweeps (termed "forward" and "backward", respectively), yielded identical results within experimental precision, consistent with the symmetry of the magnetoelastic response. Notably, the charge accumulation saturated at the same magnetic field as the magnetization rotation, confirming a direct correlation between the magnetoelectric response and magnetization orientation. The measured charge difference for the 400 μm diameter dot between fully in-plane and out-of-plane

magnetization orientations was ≈1.2 pC. We note that raw measurement data were corrected for a linear charge drift caused by the input bias current of the electrometer. Minor discrepancies in the saturation region between positive and negative bias voltages may be attributed to inherent limitations in the drift correction process, resulting in slight residual variations in the adjusted data.

The induced electric polarization (expressed as an open circuit voltage difference ΔV_{ME}) between in-plane and out-of-plane magnetization states across the PVDF-TrFE capacitor was determined by dividing the measured charge difference by the experimental capacitance at zero bias (C_0). For the specific dot dimension of 400 µm, this resulted in $\Delta V_{ME} = 46 \pm 4$ mV. Notably, this open circuit voltage difference was significantly smaller than the ferroelectric coercive voltages, justifying the approximation of constant capacitance at zero bias.

The measurement of dots with different diameters further allowed for the assessment of area scaling of the induced charges and open circuit voltages. While a more detailed study using finite element simulations will be presented below, ignoring elastic and dielectric edge effects in a planar capacitor geometry leads to simplified expressions for charge, polarization, and open circuit voltage differences between in-plane and out-of-plane magnetization states:

$$\Delta Q = A \cdot d_{33} \cdot \lambda \cdot Y \tag{2}$$

$$\Delta P_{ME} = \Delta Q / A = d_{33} \cdot \lambda \cdot Y \tag{3}$$

$$\Delta V_{ME} = t \cdot d_{33} \cdot \kappa^{-1} \cdot \lambda \cdot Y \tag{4}$$

Here, A is the area of the capacitor, λ the magnetostrictive saturation strain of the Ni foil, whereas t, d_{33}, κ, and Y are the thickness, the piezoelectric charge coefficient, the dielectric constant, and the Young's modulus of the PVDF-TrFE film, respectively. The equations indicate that the charge accumulation should increase linearly with capacitor area (quadratically with dot diameter), whereas the generated polarization and open circuit voltage differences are area independent. As depicted in Figure 3d, the charge difference (ΔQ) exhibits a positive correlation with the dot diameter, demonstrating a clear increasing trend. Conversely, the data in Figure 3e, showing voltage and polarization differences, demonstrate rather a decreasing trend with increasing dot diameter. However. it is important to note that the preceding equations were derived under the assumption of complete uniform strain transfer within the piezoelectric layer, a condition that may not completely hold for the present geometry. Moreover, increasing leakage currents due to defects in the larger dots may also contribute to the reduction of accumulated charge per area and voltage. To address this, a more comprehensive analysis of the area dependence, based on finite element simulations, will be discussed in the subsequent section.

From these measurements for a 550 nm thick PVDF-TrFE film, we obtained a maximum polarization difference between in-plane and out-of-plane magnetization orientation for the 250 µm dot of $\Delta P_{ME} = (13.8 \pm 0.8) \times 10^{-4}$ µCcm^{-2}, which corresponds to an open circuit voltage difference of $\Delta V_{ME} = (75 \pm 6)$ mV. By contrast, the minimum values in our experiments were $\Delta P_{ME} = (6.0 \pm 0.3) \times 10^{-4}$ µCcm^{-2} and $\Delta V_{ME} = 36 \pm 2$ mV, obtained for the 750 µm dot.

The experimental data allow us to estimate a magnetoelectric coupling coefficient for the PVDF-TrFE/Ni bilayers, defined as

$$\alpha_{ME} = \frac{\Delta V_{ME}}{t \cdot \mu_0 H} \tag{5}$$

where μ_0 is the vacuum permeability. This yields coupling coefficients in the range from $(1.1 \pm 0.1) \times 10^5$ Vm^{-1}T^{-1} to $(2.3 \pm 0.2) \times 10^5$ Vm^{-1}T^{-1}, depending on the dot diameter, up to the magnetic field at which the out-of-plane magnetization saturates. Notably, this value is smaller than those observed for in-plane magnetic fields[49–52] due to the presence of strong demagnetization fields and the resulting low magnetic susceptibility in our configuration. Enhancing the permeability through the selection of magnetostrictive materials with reduced shape anisotropy near the transition to perpendicular anisotropy, such as tailored Co/Ni multilayers, could potentially address this limitation, although this is beyond the scope of this work. A more direct comparison of magnetoelectric coupling coefficients that is less dependent on geometry can be achieved by defining the magnetoelectric response with respect to magnetization rather than applied field as

$$\alpha_{ME}^{M} = \frac{1}{\chi} \alpha_{ME} \tag{6}$$

with the magnetic susceptibility χ. In our geometry, the susceptibility of the magnetic component of the magnetostrictive composite $\chi = 1$ up to the saturation field, leading to values of α_{ME}^{M} between 150 ± 12 mVA^{-1} for the 750 µm dot and 310 ± 27 mVA^{-1} for the 250 µm dot. These magnetoelectric coefficients for PVDF-TrFE/Ni are around one to two orders of magnitude larger than those reported in previous studies employing small-signal AC magnetic measurements on in-plane magnetized Ni foils combined with various piezoelectric thin films ($Pb[Zr_xTi_{1-x}]O_3$, $Ba[Zr_xTi_{1-x}]O_3$-$[Ba_xCa_{1-x}]TiO_3$, or AlN).[49–52] This difference can be attributed to improved material parameters but mainly to the adverse impact of magnetic domain formation near zero in-plane magnetic field in previous studies, which strongly reduces the magnetostrictive response of the ferromagnetic substrate. This effect is much less pronounced in the out-of-plane configuration employed here.

3. Finite Element Simulations of Magnetoelectric Capacitors

3.1. Scaling of PVDF-TrFE/Ni Magnetoelectric Capacitors

A primary objective in magnetoelectric research for microelectronics is the characterization of device properties at the nanoscale. However, experimental investigations of miniaturized magnetoelectric devices pose significant challenges due to the rapid reduction of the generated charge below the measurement sensitivity threshold for PVDF-TrFE/Ni capacitors with diameters <≈100 µm. While multi-dot arrays can potentially enhance sensitivity, they introduce additional issues related to leakage current control and require complex contacting schemes. Alternatively,

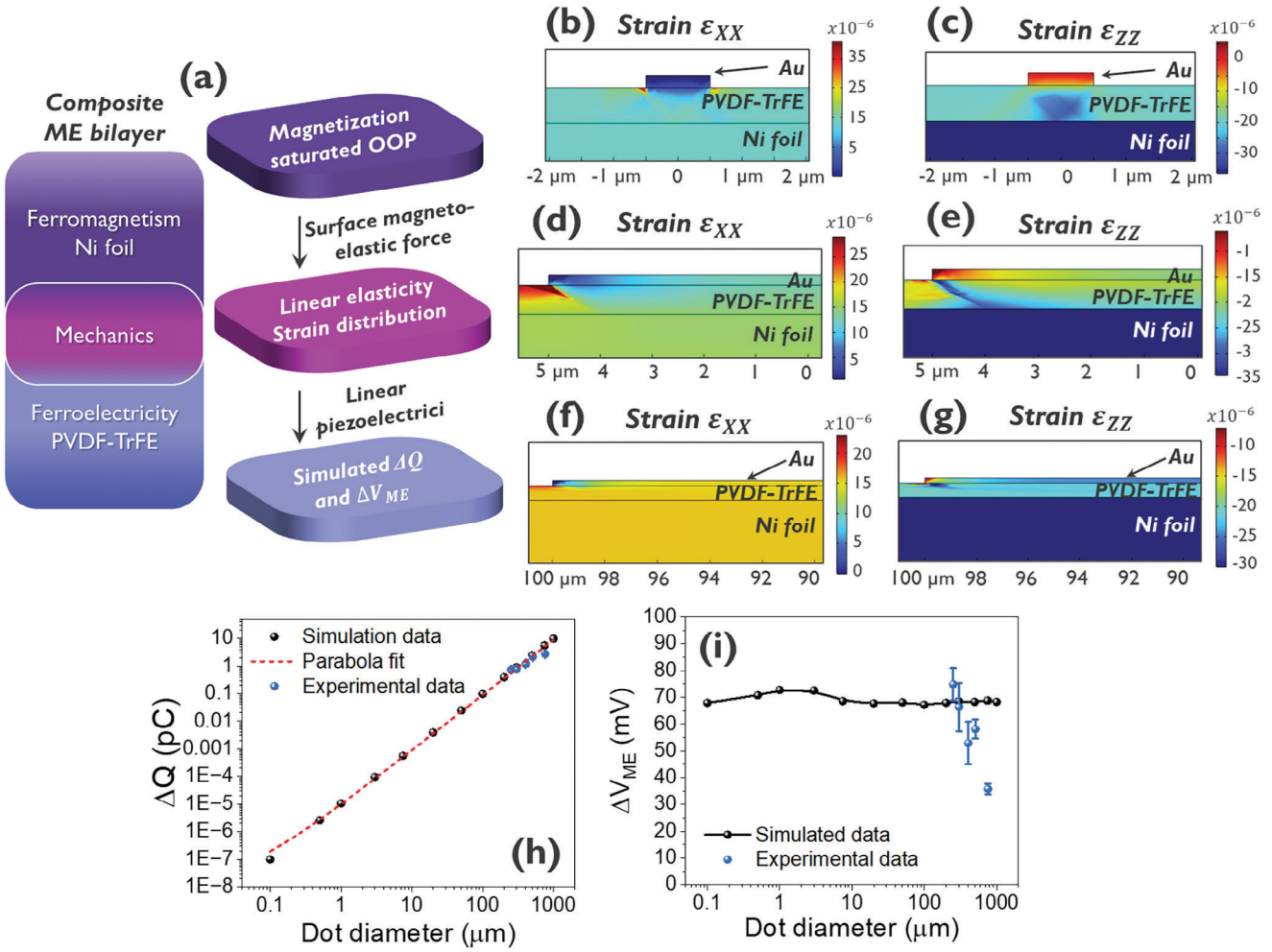

Figure 4. Finite element simulations of direct magnetoelectric effects in PVDF-TrFE/Ni bilayer composites. a) Schematic of the COMSOL Multiphysics simulation framework. b–g) Spatial distributions of in-plane (ϵ_{xx}) and out-of-plane (ϵ_{zz}) normal strain components for different Au top electrode diameters: (b,c) 1 μm, (d,e) 10 μm, (f,g) 200 μm. The results show that strain transfer from Ni to PVDF-TrFE increases with larger Au electrodes, but is limited by strain relaxation at the edges. h,i) Simulated charge accumulation (ΔQ) and magnetoelectric polarization (open circuit voltage) difference (ΔV_{ME}) as a function of Au electrode diameter, demonstrating reasonable agreement with experimental data without adjustable material parameters.

readout transistors also offer the potential to improve sensitivity, but the (monolithic) integration of scaled magnetoelectric devices with similarly scaled transistors remains a complex experimental challenge. Consequently, in this work, we have employed finite element simulations, calibrated against experimental data, to assess the scalability of PVDF-TrFE/Ni capacitors to nanoscale lateral dimensions. This modeling approach further enables the assessment of the validity of Equations (2)–(4) in the presence of elastic and electrical nonideality and can provide insight into the operation of the devices.

Finite element simulations were carried out using COMSOL Multiphysics to characterize the elastic response of Au/PVDF-TrFE/Ni capacitors, predict magnetoelectric polarization as well as open circuit voltage and charge differences, and evaluate the effects of dimensional scaling. The static magnetoelectric effect was modeled under the assumption of uniform magnetization within the Ni foil, neglecting magnetic domain formation due to the applied magnetic field configuration. **Figure** 4a depicts the simulation framework. Saturated out-of-plane magnetization and the ensuing magnetostrictive (saturation) strain were simulated by applying a surface magnetoelastic force to the magnetostrictive layer. The resulting strain distribution in the magnetostrictive and piezoelectric layers was determined using linear elasticity, which was coupled to the electrostatic response via a linear piezoelectric model to calculate charge accumulation and generated polarization. All material parameters used in the simulations are listed in **Table** 1.

Figure 4b,c illustrate the calculated in-plane (ϵ_{xx}) and out-of-plane (ϵ_{zz}) normal strain distributions for a 1 μm wide Au top electrode, respectively. According to Equation (1), an out-of-plane magnetic field induces an out-of-plane uniaxial strain in the Ni substrate, resulting in an out-of-plane tetragonal distortion. The simulations find nearly complete strain transfer from Ni to the PVDF-TrFE film. The relaxed Au electrode induces a minor reduction in in-plane strain near the electrode-PVDF-TrFE interface due to clamping. At the electrode corners, nanoindentation effects lead to an increase in in-plane strain ϵ_{xx} and the generation of shear strain (not shown) at the top of the PVDF-TrFE layer.

Table 1. Material parameters for COMSOL Multiphysics simulations. For Ni and Terfenol-D, the magnetostriction coefficients b_1 and b_2 are equal, thus only b_1 is listed. Parameters without specified sources were obtained from the COMSOL Multiphysics Material Library. Values marked with an asterisk (*) were determined experimentally.

Material	Young's modulus [GPa]	Poisson ratio	Relative permittivity κ	Piezoelectric coefficient d_{33} [pC N^{-1}]	Saturation magnetostriction λ [ppm]	b_1 [MPa]
Ni[55,56]	200	0.31	-	-	50	10
PVDF-TrFE	3.6[57]	0.4[57]	11.4*	−58[47]	-	-
Au	70	0.44	-	-	-	-
Terfenol-D[58–60]	70	0.25	-	-	1690	118
ScAlN[61]	185	0.33	16.0*	−26.3	-	-

Additionally, the presence of the Au electrode enhances the out-of-plane strain ϵ_{zz} in the underlying PVDF-TrFE layer, potentially increasing the piezoelectric polarization due to clamping.

Increasing the Au electrode diameter significantly alters the strain distribution within the system. Figure 4d,e present views of the calculated ϵ_{xx} and ϵ_{zz} distributions around the outer part of a 10 µm wide Au electrode. These results demonstrate that the Au electrode is strained at its center, with complete strain transfer from the Ni substrate to both the PVDF-TrFE film and the Au electrode. Near the electrode edges, strain relaxation occurs due to free sidewalls, which locally enhances the out-of-plane strain in the PVDF-TrFE layer, qualitatively similar to the case of the 1 µm Au electrode. Nanoindentation effects increase the surface in-plane strain in the PVDF-TrFE layer outside the electrode close to its edges, again qualitatively similar to the observations for the 1 µm Au electrode.

Lastly, we examine the calculated ϵ_{xx} and ϵ_{zz} distributions for a 200 µm wide Au top electrode, as shown in Figure 4f,g, respectively. Similar to the 10 µm wide Au electrode, complete strain transfer from the Ni foil to both the PVDF-TrFE layer and the Au electrode occurs at the electrode center. Again, strain relaxation due to free sidewalls can be observed near the electrode edges. For dot diameters significantly larger than the edge relaxation length scales, the strain within the structures can be accurately approximated as uniform, validating Equations (2)–(4).

A comparison between the calculated charge accumulation (Figure 4h) between in-plane and out-of-plane magnetization orientations with the experimental data presented in the preceding section shows reasonable agreement without the need for adjustable parameters, in particular for the smallest dot diameters. The simulation results indicate quadratic area scaling of the accumulated charge down to the smallest areas (Figure 4h), in keeping with the case of uniform strain described by Equation (2).

As depicted in Figure 4i, the simulated voltage differences corroborate the overall scaling behavior. Notably, the voltage difference exhibits only a minimal dependence on the electrode area. The slight variation can be attributed to the influence of the Au electrode and its diameter-dependent strain state, as discussed above. For dot electrodes exceeding 50 µm, the strain within the PVDF-TrFE layer can be assumed to be uniform, resulting in a diameter-independent device response. Conversely, for smaller dot electrodes ranging from 1 to 50 µm, a slightly larger voltage difference is observed, likely due to edge relaxation effects in the top electrode, which tend to increase the out-of-plane strain in the underlying PVDF-TrFE layer. Finally, for the smallest diameters below 1 µm, a modest decrease in the voltage difference with decreasing Au electrode diameter is observed, potentially attributable to nanoindentation phenomena. Overall, the simulations clearly demonstrate the scalability of these devices, exhibiting quadratic area scaling of the generated charge and minimal variations in polarization a wide range of lateral dimensions, down to the 100 nm scale.

For the smallest dot diameters, the experimentally measured voltage differences also agree well with the simulated values within the measurement accuracy, without the need for adjustable parameters. For larger dots with diameters exceeding 300 µm, the experimental charge density and open circuit voltage differences progressively fall below the simulated values, although they remain within the same order of magnitude. This discrepancy can be attributed to the presence of leakage currents through the PVDF-TrFE film, possibly due to an increasing number of (localized) leakage pathways in larger dots, resulting in a reduction of the measured charge per area and consequently to reduced polarization differences. This is also consistent with the observed lower device yield for the largest dots with 750 µm diameter. In general, however, the reasonable correlation between simulations and experimental results provides robust validation of the simulation framework.

3.2. Finite Element Simulations Scaled Magnetoelectric Devices: High Polarization and Charge Accumulation at Nanometer Lateral Dimensions

The eventual integration of scaled magnetoelectric devices with conventional complementary metal-oxide-semiconductor (CMOS circuitry on Si substrates is essential for microelectronic applications.[34,35] Large, micrometer-sized devices employing both magnetostrictive and piezoelectric thin films on rigid substrates suffer from substrate clamping effects, leading often to a strong reduction in magnetoelectric response. Mitigating this challenge requires miniaturization of device lateral dimensions and an increase in aspect ratio to facilitate unconstrained motion of sidewalls. While optimization of magnetoelectric coupling in macroscopic devices relies primarily on tailoring piezoelectric and magnetostrictive material parameters, nanoscale devices exhibit also a strong dependence on structural dimensions as well as on the mechanical properties of the surroundings. Consequently, finite element simulations are necessary for accurate device characterization due to the pronounced influence of non-idealities, such as nanoindentation or local clamping effects.

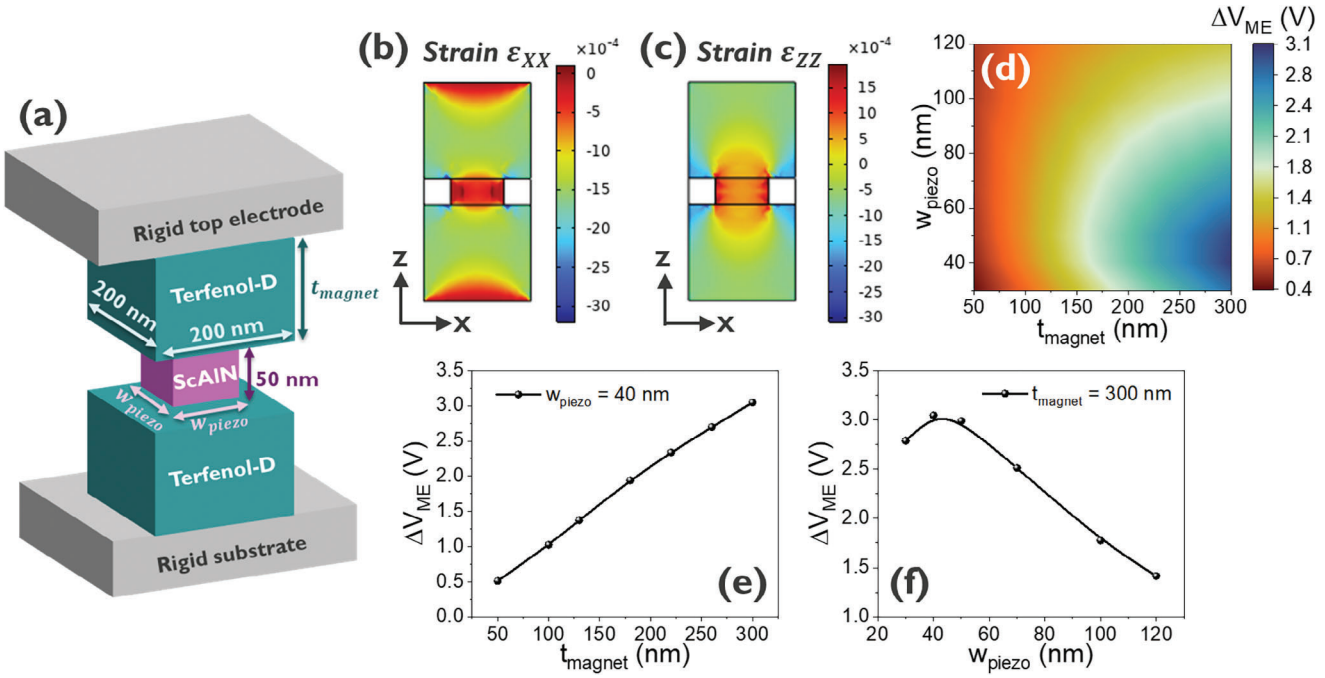

Figure 5. a) Schematic representation of a nanoscale piezoelectric device with a 50 nm thick ScAlN layer sandwiched between two Terfenol-D layers of variable thickness. b,c) Spatial distributions of in-plane (ϵ_{xx}) and out-of-plane (ϵ_{zz}) normal strains in the ScAlN layer when the magnetization is oriented out of plane. Simulated strains reach 500 ppm for ϵ_{xx} and 1500 ppm for ϵ_{zz}. d) Simulated open circuit voltage difference ΔV_{ME} between in-plane and out-of-plane magnetization orientations, exceeding 2 V in range of parameters studied here. e,f) Simulated ΔV_{ME} as a function of Terfenol-D thickness (e, ScAlN width of 40 nm) and ScAlN lateral dimension (f, Terfenol-D thickness of 300 nm).

Using this approach, we have designed a nanoscale magnetoelectric device,[62] similar to piezoelectric transistor architectures,[63,64] and simulated its performance using the calibrated COMSOL model described above. This device, depicted schematically in **Figure** 5a, comprises a piezoelectric pillar sandwiched between two magnetostrictive elements, which also function as electrodes if metallic. Material optimization, considering the material properties as well as their CMOS-compatibility, led to the selection of ScAlN ($Sc_{0.4}Al_{0.6}N$) as the piezoelectric and Terfenol-D ($Tb_{0.3}Dy_{0.7}Fe_2$) as the magnetostrictive component. Both materials can be deposited in form of polycrystalline thin films using techniques (e.g., PVD) compatible with CMOS manufacturing. While the lateral dimensions of the magnetostrictive element were constant (200 nm) and its thickness was varied in the simulations, the thickness of the piezoelectric element remained constant (50 nm) and its lateral dimensions were variable. To optimize strain transfer,[64,65] the device's top and bottom surfaces were assumed to be mechanically constrained, which could be achieved in practice by encapsulating the device by surrounding layers with a high Young's modulus such as TiN or diamond. Finite element simulations within the previously described framework were then used to calculate the mechanical response as well as voltage differences between in-plane and out-of-plane magnetization orientations. Figure 5b,c illustrate the resulting strain distributions, revealing substantial strain generation within the piezoelectric element and notable backaction effects on the magnetostrictive electrodes, particularly near the piezoelectric element corners, due to nanoindentation.

The simulated voltage differences depicted in Figure 5d show substantial induced polarization differences, equivalent to open circuit voltage differences exceeding 2 V, for scaled devices with nanometer dimensions comparable to, e.g., those of state-of-the-art MRAM cells. The data underscore the dominant influence of device dimensions on device performance, in particular of the magnet thickness (Figure 5e), with the width (aspect ratio) of the piezoelectric element also contributing significantly (Figure 5f). These findings highlight the promising potential of magnetoelectric devices for spintronic applications, due to the possibility to generate large CMOS-compatible open circuit voltages at scaled dimensions, even on rigid substrates.

4. Conclusion

In conclusion, we have experimentally investigated the magnetoelectric coupling in PVDF-TrFE/Ni bilayers by directly measuring the charge accumulation (ΔQ) induced by out-of-plane magnetization rotation via an applied magnetic field. The observed device response exhibited no dependence on magnetic field polarity or sweep direction, consistent with the expected behavior of magnetoelectric coupling. Measurements found maximum polarization differences (ΔP_{ME}) between in-plane and out-of-plane magnetization orientations of up to $(13.8 \pm 0.8) \times 10^{-4}$ μCcm^{-2}. This value was equivalent to an open circuit voltage difference (ΔV_{ME}) of 75 ± 6 mV, using measured capacitances. To compensate for the low near-unity permeability associated with strong demagnetizing fields in the present configuration, magnetoelectric coupling coefficients were determined with respect to magnetization

rather than magnetic field, yielding a maximum value of 310 ± 27 mVA^{-1}. This represents approximately a one to two orders of magnitude increase compared to previously reported values for Ni foil/thin film piezoelectric in in-plane geometries.[49–52]

Finite element simulations using COMSOL Multiphysics corroborated the experimental results regarding charge accumulation and voltage differences in PVDF-TrFE/Ni bilayer capacitors. A good agreement was in general observed between simulated and experimental results. Moreover, simulations demonstrated the scalability of the devices, with minimal (within 10%) variation in open circuit voltage differences across different lateral dimensions down to the 100 nm range. Minor deviations could be ascribed to edge effects and clamping induced by the Au top electrodes. Additional simulations using optimized materials and structures, employing Terfenol-D and ScAlN as magnetostrictive and piezoelectric materials, respectively, predicted large open circuit voltage differences exceeding 2 V for nanoscale devices on rigid substrates.

These findings highlight the potential of magnetoelectric materials to generate substantial polarization and charge accumulation. Despite the potential for ultralow power spintronic logic,[9,66–69] the inefficiencies inherent in the transduction between magnetic and electric domain currently counterbalance all anticipated benefits due to utilizing magnetic excitations rather than charge carriers for computation.[34] Consequently, the realization of scaled magnetoelectric readout devices would constitute a major advance for spintronic applications,[9] enabling potentially faster readout at lower power. Coupling such devices, e.g., to gates of scaled transistors, which can be turned on or off by the magnetoelectric charge, has the potential for large magnetoresistive effects that can be used, e.g., in spintronic logic circuits.

However, experimental characterization of scaled devices is hindered by the generation of small charge quantities, necessitating either the processing of large-scale multi-device arrays or the integration with transistors or CMOS-based sense amplifiers. Addressing these challenges through the practical implementation and the experimental study of the simulated optimized structures will constitute a crucial step toward developing spintronic circuits that offer competitive throughput and area efficiency while operating at significantly reduced power levels.

5. Experimental Section

Preparation of Ferroelectric PVDF-TrFE: Ferroelectric β-phase PVDF-TrFE films were fabricated through a four-step process: solution preparation, spin coating, thermal annealing, and electric poling. A solution of a PVDF-TrFE power (30% TrFE, Piezotech FC30) in methyl ethyl ketone (MEK) was prepared at a concentration of 55 mg mL^{-1}. Spin coating at 4000 rpm for 30 seconds yielded a 550 nm thick polymer layer on the desired substrate (Si or Ni foil). It was noted that thinner PVDF-TrFE increased the risk pinhole formation and excessive leakage currents, especially on the rough Ni foil. Conversely, much thicker films would have necessitated higher poling voltages outside the capabilities of the setup. Subsequent thermal annealing under vacuum at 70 °C for 4.5 h, followed by curing in a nitrogen environment at 140 °C for 1 h, enhanced the film quality. The thickness of PVDF-TrFE films was calibrated on Si substrates using spectroscopic ellipsometry (J.A. Woolam RC2) and verified using a Bruker Dektak XT profilometer. Finally, electric poling with 80 V peak-to-peak triangular waveforms at 50 Hz for 200 pulses induced the phase transition from the non-polar α- to the ferroelectric β-phase.[45]

Sample Characterization: Optical microscopy of the fabricated devices was performed using a Nikon Eclipse L200 microscope. The surface morphology of the PVDF-TrFE layer was characterized by atomic force microscopy (AFM) using a Bruker Dimension Edge instrument. Ferromagnetic properties of the Ni foils were investigated by magnetization–magnetic field (M–H) hysteresis loop measurements employing a MicroSense EV11 vibrating sample magnetometer (VSM). In-plane and out-of-plane magnetic fields were applied within ranges of ±0.2 T and ±1.2 T, respectively. Ferroelectric properties of the PVDF-TrFE films were assessed using a Keithley 4200A-SCS parameter analyzer for polarization-voltage (P–V) hysteresis loop measurements and electric field poling. Dielectric properties were characterized by capacitance-voltage (C–V) measurements conducted with an E4980A precision LCR meter at a frequency of 10 kHz and an AC voltage of 100 mV (RMS), applying a DC bias sweep between ±35 V.

Magnetoelectric Coupling Measurements: To characterize the magnetoelectric coupling, out-of-plane magnetic field sweeps between −1.0 and 1.0 T were applied to the PVDF-TrFE/Ni composite. The generated charge due to the magnetoelectric effect was simultaneously measured using a Keithley 6517B Electrometer. While this instrument exhibits an exceptionally low input bias current, long-term integration resulted in a measurable charge drift.[70] This systematic error was corrected by subtracting a linear charge drift, attributed to the input bias current, from the raw measurement data.

Finite Element Modeling: COMSOL Multiphysics was employed to simulate strain, charge, and voltage generation within PVDF-TrFE/Ni foil composites as well as in scaled Terfenol-D/ScAlN devices due to the magnetoelectric effect. The model adopted a simplified approach, representing magnetostriction as a surface force acting on the magnetic surface. This surface magnetoelastic force was calculated using the formula:

$$f_{mec} = -n \begin{pmatrix} b_1 m_x^2 & b_2 m_x m_y & b_2 m_x m_z \\ b_2 m_x m_y & b_1 m_y^2 & b_2 m_y m_z \\ b_2 m_x m_z & b_2 m_y m_z & b_1 m_z^2 \end{pmatrix} \quad (7)$$

where $n = \{n_x, n_y, n_z\}$ is the unit vector normal to the boundary, b_1 and b_2 are magnetostriction materials constants, and $m = \{m_x, m_y, m_z\}$ is the normalized magnetization direction vector.[71,72] The simulations assume a uniform magnetization distribution within the magnetic film and neglect transient effects, i.e., $\partial m/\partial t = 0$. Additionally, the piezoelectric behavior of the PVDF-TrFE layer was modeled under the assumption of linear piezoelectricity.

Material parameters for Au employed in the simulations were obtained from the COMSOL Multiphysics Material Library. Mechanical and piezoelectric properties of PVDF-TrFE and ScAlN, and all the material parameters for Ni and Terfenol-D were sourced from previous literature reports.[47,55–61] Lastly, dielectric parameters for PVDF-TrFE and ScAlN were experimentally determined. A comprehensive list of material properties is provided in Table 1.

Acknowledgements

F.L. and E.G. contributed equally to this work. This work has been supported by imec's industrial affiliate program on exploratory logic. F.L. and E.V.M. acknowledge support by the Research Foundation Flanders (Fonds Wetenschappelijk Onderzoek, FWO) through PhD fellowships under grant agreements No. 1183722N and No. 1SH4Q24N, respectively.

Conflict of Interest

The authors declare no conflict of interest.

Data Availability Statement

The data that support the findings of this study are available from the corresponding author upon reasonable request.

Keywords

Magnetoelectric effect, magnetostriction, Ni, piezoelectricity, PVDF-TrFE, thin-film magnetoelectric composites

Received: November 20, 2024
Published online: January 29, 2025

[1] M. Fiebig, *J. Phys. D: Appl. Phys.* **2005**, *38*, R123.
[2] W. Eerenstein, N. D. Mathur, J. F. Scott, *Nature* **2006**, *442*, 759.
[3] S.-W. Cheong, M. Mostovoy, *Nat. Mater.* **2007**, *6*, 13.
[4] C.-W. Nan, M. I. Bichurin, S. Dong, D. Viehland, G. Srinivasan, *J. Appl. Phys.* **2008**, *103*, 031101.
[5] N. A. Spaldin, R. Ramesh, *Nat. Mater.* **2019**, *18*, 203.
[6] X. Liang, A. Matyushov, P. Hayes, V. Schell, C. Dong, H. Chen, Y. He, A. Will-Cole, E. Quandt, P. Martins, J. McCord, M. Medarde, S. Lanceros-Mendez, S. van Dijken, N. X. Sun, J. Sort, *IEEE Trans. Magn.* **2021**, *57*, 400157.
[7] M. Mostovoy, *npj Spintronics* **2024**, *2*, 18.
[8] H. Béa, M. Gajek, M. Bibes, A. Barthélémy, *J. Phys.: Condens. Matter* **2008**, *20*, 434221.
[9] S. Manipatruni, D. E. Nikonov, I. A. Young, *Nat. Phys.* **2018**, *14*, 338.
[10] S. Manipatruni, D. E. Nikonov, C.-C. Lin, T. A. Gosavi, H. Liu, B. Prasad, Y.-L. Huang, E. Bonturim, R. Ramesh, I. A. Young, *Nature* **2019**, *565*, 35.
[11] A. Mahmoud, F. Ciubotaru, F. Vanderveken, A. V. Chumak, S. Hamdioui, C. Adelmann, S. Cotofana, *J. Appl. Phys.* **2020**, *128*, 161101.
[12] Y.-H. Chu, L. W. Martin, M. B. Holcomb, M. Gajek, S.-J. Han, Q. He, N. Balke, C.-H. Yang, D. Lee, W. Hu, Q. Zhan, P.-L. Yang, A. Fraile-Rodríguez, A. Scholl, S. X. Wang, R. Ramesh, *Nat. Mater.* **2008**, *7*, 478.
[13] F. Matsukura, Y. Tokura, H. Ohno, *Nat. Nanotech.* **2015**, *10*, 209.
[14] B. Prasad, Y.-L. Huang, R. V. Chopdekar, Z. Chen, J. Steffes, S. Das, Q. Li, M. Yang, C.-C. Lin, T. Gosavi, D. E. Nikonov, Z. Q. Qiu, L. W. Martin, B. D. Huey, I. Young, J. Íñiguez, S. Manipatruni, R. Ramesh, *Adv. Mater.* **2020**, *32*, 2001943.
[15] R. Ramesh, N. A. Spaldin, *Nat. Mater.* **2007**, *6*, 21.
[16] G. Catalan, J. F. Scott, *Adv. Mater.* **2009**, *21*, 2463.
[17] J. T. Heron, D. G. Schlom, R. Ramesh, *Appl. Phys. Rev.* **2014**, *1*, 021303.
[18] J. A. Mundy, C. M. Brooks, M. E. Holtz, J. A. Moyer, H. Das, A. F. Rébola, J. T. Heron, J. D. Clarkson, S. M. Disseler, Z. Liu, A. Farhan, R. Held, R. Hovden, E. Padgett, Q. Mao, H. Paik, R. Misra, L. F. Kourkoutis, E. Arenholz, A. Scholl, J. A. Borchers, W. D. Ratcliff, R. Ramesh, C. J. Fennie, P. Schiffer, D. A. Muller, D. G. Schlom, *Nature* **2016**, *537*, 523.
[19] N. A. Hill, *J. Phys. Chem. B* **2000**, *104*, 6694.
[20] C. Ederer, N. A. Spaldin, *Phys. Rev. B* **2005**, *71*, 060401.
[21] S. Priya, R. Islam, S. Dong, D. Viehland, *J. Electroceram.* **2007**, *19*, 149.
[22] M. I. Bichurin, D. Viehland, G. Srinivasan, *J. Electroceram.* **2007**, *19*, 243.
[23] J. Ma, J. Hu, Z. Li, C. Nan, *Adv. Mater.* **2011**, *23*, 1062.
[24] M. Liu, N. X. Sun, *Philos. Trans. R. Soc. A* **2014**, *372*, 20120439.
[25] A. K. Biswas, H. Ahmad, J. Atulasimha, S. Bandyopadhyay, *Nano Lett.* **2017**, *17*, 3478.
[26] S. Zhang, Y. Zhao, X. Xiao, Y. Wu, S. Rizwan, L. Yang, P. Li, J. Wang, M. Zhu, H. Zhang, X. Jin, X. Han, *Sci. Rep.* **2014**, *4*, 3727.
[27] S.-W. Yang, R.-C. Peng, T. Jiang, Y.-K. Liu, L. Feng, J.-J. Wang, L.-Q. Chen, X.-G. Li, C.-W. Nan, *Adv. Mater.* **2014**, *26*, 7091.
[28] P. Li, A. Chen, D. Li, Y. Zhao, S. Zhang, L. Yang, Y. Liu, M. Zhu, H. Zhang, X. Han, *Adv. Mater.* **2014**, *26*, 4320.
[29] W. Zhao, J. Kim, X. Huang, L. Zhang, D. Pesquera, G. A. P. Velarde, T. Gosavi, C.-C. Lin, D. E. Nikonov, H. Li, I. A. Young, R. Ramesh, L. W. Martin, *Adv. Funct. Mater.* **2021**, *31*, 2105068.
[30] J. T. Heron, J. L. Bosse, Q. He, Y. Gao, M. Trassin, L. Ye, J. D. Clarkson, C. Wang, J. Liu, S. Salahuddin, D. C. Ralph, D. G. Schlom, J. Íñiguez, B. D. Huey, R. Ramesh, *Nature* **2014**, *516*, 370.
[31] P. Debashis, J. J. Plombon, C.-C. Lin, Y.-C. Liao, H. Li, D. E. Nikonov, D. Adams, C. Rogan, M. Dc, M. Radosavljevic, S. B. Clendenning, I. A. Young, In *Proc. 2022 IEEE Intern. Electron Devices Meet. (IEDM)*, **2022**, https://doi.org/10.1109/IEDM45625.2022.10019505.
[32] G. Srinivasan, *Ann. Rev. Mater. Res.* **2010**, *40*, 153.
[33] D. Viehland, J. F. Li, Y. Yang, T. Costanzo, A. Yourdkhani, G. Caruntu, P. Zhou, T. Zhang, T. Li, A. Gupta, M. Popov, G. Srinivasan, *J. Appl. Phys.* **2018**, *124*, 061101.
[34] J. A. C. Incorvia, T. P. Xiao, N. Zogbi, A. Naeemi, C. Adelmann, F. Catthoor, M. Tahoori, F. Casanova, M. Becherer, G. Prenat, S. Couet, *Nat. Rev. Electr. Eng.* **2024**, *1*, 700.
[35] R. Ramesh, S. Salahuddin, S. Datta, C. H. Diaz, D. E. Nikonov, I. A. Young, D. Ham, M.-F. Chang, W.-S. Khwa, A. S. Lele, C. Binek, Y.-L. Huang, Y.-C. Sun, Y.-H. Chu, B. Prasad, M. Hoffmann, J.-M. Hu, Z. (Jackie) Yao, L. Bellaiche, P. Wu, J. Cai, J. Appenzeller, S. Datta, K. Y. Camsari, J. Kwon, J. A. C. Incorvia, I. Asselberghs, F. Ciubotaru, S. Couet, C. Adelmann, et al., *APL Mater.* **2024**, *12*, 099201.
[36] F. Meng, S.-Y. Lee, O. Zografos, M. Gupta, V. D. Nguyen, G. D. Micheli, S. Cotofana, I. Asselberghs, C. Adelmann, G. S. Kar, S. Couet, F. Ciubotaru, *IEEE Trans. Circuits Syst. I: Regul. Pap.* **2024**, https://doi.org/10.1109/TCSI.2024.3420250.
[37] S. O. Valenzuela, M. Tinkham, *Nature* **2006**, *442*, 176.
[38] Y. Omori, F. Auvray, T. Wakamura, Y. Niimi, A. Fert, Y. Otani, *Appl. Phys. Lett.* **2014**, *104*, 242415.
[39] C.-C. Lin, T. Gosavi, D. Nikonov, Y.-L. Huang, B. Prasad, W. Choi, V. T. Pham, I. Groen, J.-Y. Chen, M. D. C., H. Liu, K. Oguz, E. S. Walker, J. Plombon, B. Buford, C. H. Naylor, J.-P. Wang, F. Casanova, R. Ramesh, I. A. Young, in *Proc. 2019 IEEE Intern. Electron Devices Meet. (IEDM)*, **2019**, https://doi.org/10.1109/IEDM19573.2019.8993620.
[40] V. T. Pham, I. Groen, S. Manipatruni, W. Y. Choi, D. E. Nikonov, E. Sagasta, C.-C. Lin, T. A. Gosavi, A. Marty, L. E. Hueso, I. A. Young, F. Casanova, *Nat. Electron* **2020**, *3*, 309.
[41] D. C. Vaz, C.-C. Lin, J. J. Plombon, W. Y. Choi, I. Groen, I. C. Arango, A. Chuvilin, L. E. Hueso, D. E. Nikonov, H. Li, P. Debashis, S. B. Clendenning, T. A. Gosavi, Y.-L. Huang, B. Prasad, R. Ramesh, A. Vecchiola, M. Bibes, K. Bouzehouane, S. Fusil, V. Garcia, I. A. Young, F. Casanova, *Nat. Commun.* **2024**, *15*, 1902.
[42] G. Gutiérrez-Sánchez, J. Hernando-García, V. Ruiz-Diez, O. J. Dura, M. A. López de la Torre, J. L. Sánchez-Rojas, in *Smart Sensors, Actuators, and MEMS VIII*, Vol. *10246*, (Eds.: L. Fonseca, M. Prunnila, E. Peiner), SPIE, Barcelona, Spain, **2017**, pp. 148–153.
[43] N. Sulitanu, *J. Magn. Magn. Mater.* **1992**, *113*, 238.
[44] C. Ribeiro, C. M. Costa, D. M. Correia, J. Nunes-Pereira, J. Oliveira, P. Martins, R. Gonçalves, V. F. Cardoso, S. Lanceros-Méndez, *Nat. Protoc.* **2018**, *13*, 681.
[45] B. Liang, L. Paquet, Y. Jeong, P. Heremans, D. Cheyns, in *Proc. 2021 IEEE 16th Intern. Conf. Nano/Micro Engin. Molec. Sys. (NEMS)* **2021**, p. 1423, https://doi.org/10.1109/NEMS51815.2021.9451478.
[46] D. Mao, B. E. Gnade, M. A. Quevedo-Lopez, in *Ferroelectrics – Physical Effects* (Ed.: M. Lallart), InTech, Rijeka, Croatia **2011**.
[47] A. Aliane, M. Benwadih, B. Bouthinon, R. Coppard, F. Domingues-Dos Santos, A. Daami, *Org. Electron.* **2015**, *25*, 92.
[48] X. Li, Y. Wang, T. He, Q. Hu, Y. Yang, *J. Mater. Sci.: Mater. Electron.* **2019**, *30*, 20174.
[49] H. Palneedi, H. G. Yeo, G.-T. Hwang, V. Annapureddy, J.-W. Kim, J.-J. Choi, S. Trolier-McKinstry, J. Ryu, *APL Mater.* **2017**, *5*, 096111.
[50] A. B. Swain, M. Rath, S. Dinesh Kumar, M. S. Ramachandra Rao, V. Subramanian, P. Murugavel, *J. Phys. D: Appl. Phys.* **2019**, *52*, 065004.

[51] T. Nguyen, Y. Fleming, P. Bender, P. Grysan, N. Valle, B. El Adib, N. Adjeroud, D. Arl, M. Emo, J. Ghanbaja, A. Michels, J. Polesel-Maris, *ACS Appl. Mater. Interf.* **2021**, *13*, 30874.
[52] M. Feng, J. Wang, J.-M. Hu, J. Wang, J. Ma, H.-B. Li, Y. Shen, Y.-H. Lin, L.-Q. Chen, C.-W. Nan, *Appl. Phys. Lett.* **2015**, *106*, 072901.
[53] I. Tiginyanu, P. Topala, V. Ursaki, Eds., *Nanostructures and Thin Films for Multifunctional Applications: Technology, Properties and Devices*, Springer International, Cham, Switzerland, **2016**.
[54] G. Gautschi, *Piezoelectric Sensorics*, Springer, Berlin Heidelberg **2002**.
[55] L. Dreher, M. Weiler, M. Pernpeintner, H. Huebl, R. Gross, M. S. Brandt, S. T. B. Goennenwein, *Phys. Rev. B – Condens. Matter Mater. Phys.* **2012**, *86*, 134415.
[56] G. Engdahl, *Handbook of Giant Magnetostrictive Materials*, Academic Press, San Diego, CA, **2000**.
[57] P. Poncet, F. Casset, A. Latour, F. Domingues Dos Santos, S. Pawlak, R. Gwoziecki, A. Devos, P. Emery, S. Fanget, *Actuators* **2017**, *6*, 18.
[58] D. B. Gopman, J. W. Lau, K. P. Mohanchandra, K. Wetzlar, G. P. Carman, *Phys. Rev. B* **2016**, *93*, 064425.
[59] M. Colussi, F. Berto, K. Mori, F. Narita, *Procedia Struct. Integr.* **2016**, *2*, 1837.
[60] Q. Wang, X. Li, C. Y. Liang, A. Barra, J. Domann, C. Lynch, A. Sepulveda, G. Carman, *Appl. Phys. Lett.* **2017**, *110*, 102903.
[61] M. A. Caro, S. Zhang, T. Riekkinen, M. Ylilammi, M. A. Moram, O. Lopez-Acevedo, J. Molarius, T. Laurila, *J. Phys.: Condens. Matter* **2015**, *27*, 245901.
[62] A. De Coster, *M.Sc.Thesis*, *Magnetoelectric Devices for Beyond CMOS Applications*, KU Leuven, Leuven, Belgium, **2024**.
[63] D. Newns, B. Elmegreen, X. Hu Liu, G. Martyna, *J. Appl. Phys.* **2012**, *111*, 084509.
[64] D. M. Newns, B. G. Elmegreen, X.-H. Liu, G. J. Martyna, *Adv. Mater.* **2012**, *24*, 3672.
[65] D. Tierno, F. Ciubotaru, R. Duflou, M. Heyns, I. P. Radu, C. Adelmann, *Microelectron. Eng.* **2018**, *187-188*, 144.
[66] D. E. Nikonov, I. A. Young, *Proc. IEEE* **2013**, *101*, 2498.
[67] D. E. Nikonov, I. A. Young, *J. Mater. Res.* **2014**, *29*, 2109.
[68] B. Dieny, I. L. Prejbeanu, K. Garello, P. Gambardella, P. Freitas, R. Lehndorff, W. Raberg, U. Ebels, S. O. Demokritov, J. Akerman, A. Deac, P. Pirro, C. Adelmann, A. Anane, A. V. Chumak, A. Hirohata, S. Mangin, S. O. Valenzuela, M. C. Onbaşlı, M. d'Aquino, G. Prenat, G. Finocchio, L. Lopez-Diaz, R. Chantrell, O. Chubykalo-Fesenko, P. Bortolotti, *Nat. Electron* **2020**, *3*, 446.
[69] R. Rothe, H. Li, D. E. Nikonov, I. A. Young, K. Choo, D. Blaauw, *IEEE J. Explor. Solid-State Comput. Devices Circuits* **2023**, *9*, 124.
[70] Keithley Low Level Measurements Handbook, 7th ed., Tektronix, Cleveland, OH Available at https://www.tek.com/en/documents/product-article/keithley-low-level-measurements-handbook-7th-edition. Accessed Dec. 2024.
[71] E. Law, Y. Li, O. Kahraman, C. A. Haselwandter, *Phys. Rev. E* **2021**, *104*, 014403.
[72] K. Yamamoto, W. Yu, T. Yu, J. Puebla, M. Xu, S. Maekawa, G. Bauer, *J. Phys. Soc. Jpn.* **2020**, *89*, 113702.